

Three-Dimensional Modeling of All-Solid-State Lithium-Ion Batteries Using Synchrotron Transmission X-ray Microscopy Tomography

To cite this article: Hamed Fathiannasab *et al* 2020 *J. Electrochem. Soc.* **167** 100558

View the [article online](#) for updates and enhancements.



Three-Dimensional Modeling of All-Solid-State Lithium-Ion Batteries Using Synchrotron Transmission X-ray Microscopy Tomography

Hamed Fathiannasab,^{1,*} Ali Ghorbani Kashkooli,¹ Tianyi Li,² Likun Zhu,^{2,**} and Zhongwei Chen^{1,**,z}

¹Department of Chemical Engineering, Waterloo Institute for Nanotechnology, Waterloo Institute for Sustainable Energy, University of Waterloo, Waterloo, ON N2L 3G1, Canada

²Department of Mechanical and Energy Engineering, Indiana University-Purdue University Indianapolis, Indianapolis, Indiana 46202, United States of America

In this study, a synchrotron transmission X-ray microscopy tomography system has been utilized to reconstruct the three-dimensional (3D) morphology of all-solid-state lithium-ion battery (ASSB) electrodes. The electrode was fabricated with a mixture of $\text{Li}(\text{Ni}_{1/3}\text{Mn}_{1/3}\text{Co}_{1/3})\text{O}_2$, $\text{Li}_{1.3}\text{Ti}_{1.7}\text{Al}_{0.3}(\text{PO}_4)_3$, and super-P. For the first time, a 3D numerical multi-physics model was developed to simulate the galvanostatic discharge performance of an ASSB, elucidating the spatial distribution of physical and electrochemical properties inside the electrode microstructure. The 3D model shows a wide range of electrochemical properties distribution in the solid electrolyte (SE) and the active material (AM) which might have a negative effect on ASSB performance. The results show that at high current rates, the void space hinders the ions' movement and causes local inhomogeneity in the lithium-ion distribution. The simulation results for electrodes fabricated under two pressing pressures reveal that higher pressure decreases the void spaces, leading to a more uniform distribution of lithium ions in the SE due to more facile lithium ion transport. The approach in this study is a key step moving forward in the design of 3D ASSBs and sheds light on the physical and electrochemical property distribution in the SE, active material, and their interface.

© 2020 The Electrochemical Society ("ECS"). Published on behalf of ECS by IOP Publishing Limited. [DOI: 10.1149/1945-7111/ab9380]

Manuscript submitted February 6, 2020; revised manuscript received May 4, 2020. Published June 29, 2020.

Supplementary material for this article is available [online](#)

List of symbols

c	Concentration (mol m^{-3})
D	Diffusion coefficient ($\text{m}^2 \text{s}^{-1}$)
F	Faraday's constant, 96487 (C mol^{-1})
i	Current density (A m^{-2})
J	Flux ($\text{mol m}^{-3} \text{s}^{-1}$)
k	Reaction rate constant ($\text{mol m}^{-2} \text{s}^{-1}$)
R	universal gas constant ($\text{J mol}^{-1} \text{K}^{-1}$)
z	Species charge number
E_{eq}	Open circuit voltage (V)
Greek	
α	Charge transfer coefficient
ε	Porosity
η	Over-potential (V)
σ	Conductivity (S m^{-1})
τ	Tortuosity
φ	potential (V)
subscript	
s	Solid active material
SE	Solid electrolyte
pos	Positive electrode
Li	Lithium
Li^+	Lithium-ion
n^-	Negative charge
r	Recombination rate
d	Dissociation rate
max	maximum
n	Solid electrolyte/solid active material interface
i	Species, either Li^+ or n^-
0	initial
superscript	
eq	Equilibrium

Lithium-ion batteries (LIBs) have dominated the electrochemical energy storage market for over a decade due to their high energy density, high design flexibility, and long cycle life;^{1,2} however, electric vehicles or medical instruments require LIBs with higher safety and a wider thermal stability range.^{3,4} All-solid-state lithium-ion batteries (ASSBs), which are based on solid electrolytes (SEs), are a safer alternative to the conventional liquid electrolyte LIBs. SEs eliminate safety concerns such as thermal runaway and electrolyte leakage of flammable liquid electrolytes.^{3,5} Moreover, SEs can facilitate the future application of high capacity anode materials such as metallic lithium⁶ and silicon⁷ by inhibiting the formation of needle-like microstructures called lithium dendrites on the surface of the lithium anode upon cycling⁸ and limiting the large expansion of the silicon anode during lithiation,⁹ thus improving their cycle lives. However, despite the clear advantages of ASSBs, critical challenges hinder their widespread application, including poor SE/solid active material (AM) interfacial contact, the low ionic conductivity of SEs, and poor electrochemical stability.³ In terms of the SE/AM interface, it is difficult to develop a robust interface due to the limited understanding of the microstructure and reaction interface in ASSBs.¹⁰ Since the two solid phases are not perfectly in contact with each other, void spaces block the ion pathways at the SE/AM interface, thus negatively affecting the ASSB performance.¹¹

Mathematical models have been proven to be an efficient way to shed light on the physical and electrochemical phenomena occurring in LIBs. Experimentally validated models can provide indispensable insight into their performance and limiting challenges. Mathematical models have been previously applied to simulate the charge/discharge performance of ASSBs,¹²⁻¹⁵ but most of these models are one dimensional (1D) and do not include the real microstructure of the electrode and SE in their modeling framework. For instance, Danilov et al. developed the first model that included 1D charge transfer kinetics at the SE/AM interface, diffusion and migration of ions in the SE, and diffusion of ions in the intercalation AM.¹³ While their model could simulate the galvanostatic charge/discharge profiles at low to moderate c-rates in good agreement with experimentally measured data,¹³ their model failed to predict the performance at high current rates. Kazemi et al. addressed this issue

*Electrochemical Society Student Member.

**Electrochemical Society Member.

^zE-mail: zhwchen@uwaterloo.ca

by defining a variable AM diffusion coefficient as a function of lithium concentration instead of an assumed constant value,¹² allowing them to simulate the voltage profiles accurately at low and high current rates up to 50 C (5 mA cm^{-2}). Raijmakers et al. improved the accuracy of the 1D model by considering mixed ionic/electronic conductivity in the positive electrode, electrical double layers at the SE/AM interfaces, and defining the ionic/electronic diffusion coefficient as a function of lithium concentration in the AM.¹⁵ With this improved model, they showed that overpotential in the SE is the main contributor to the overall voltage losses during discharge, while charge transfer losses are another major reason for battery performance losses in addition to electrical double layer losses at the SE/AM interface and diffusion in the positive electrode.¹⁵ In terms of the SE, all the aforementioned models are based on a binary electrolyte assumption and electro-neutrality in the SE; Wolff et al. tried to elucidate fundamental differences between single-ion and binary conducting electrolytes by implementing a pseudo-two dimensional (P2D) single-ion model.¹⁶ They demonstrated that a single-ion conduction cell produces higher capacity by exhibiting less voltage losses within the electrolyte. This makes the single-ion a better alternative to binary electrolytes specifically for high current and high energy (thick electrode) applications. In terms of the ASSB electrode design and microstructures, further investigation of the effects of electrode geometry and homogeneity is critical to identifying the optimal electrode structure.¹⁶ Bates et al. developed a 2D model for ASSBs to obtain lithium concentration and voltage profiles using simplified rectangle shapes.¹⁷ Clancy et al. compared the performances of ASSBs with three structures (thin film, 3D core-shell, and 3D electrodes) and showed that implementing 3D nanostructures can effectively enhance the areal energy and power density compared to a thin-film electrode.¹⁸ Although these models can simulate the charge/discharge performance, they cannot describe in detail the physical and electrochemical behavior of the ASSB; specifically, they fail to describe the effects of electrode microstructure's heterogeneity on the lithium-ion transport within the SE and AM, as well as their interface.

One way to investigate the physical and electrochemical behavior of ASSBs is to use the 3D reconstructed geometry of the ASSB electrode instead of simplified 1D or 2D geometries. In recent years, various techniques such as focused ion beam-scanning electron microscopy (FIB-SEM),^{19,20} magnetic resonance imaging (MRI),²¹ and computed tomography (CT)^{22–25} have become available to capture the real microstructures of LIB electrodes. Among them, the non-destructive CT imaging technique is extensively used to characterize the physical and morphological properties of the electrode including directional tortuosity, porosity, particle size distribution, and specific surface area.^{24,26–28} For instance, Banerjee et al. investigated the effects of compression on the permeability, diffusivity, and pressure drop using CT images.²⁹ They showed that the compression resulted in a 58% reduction in permeability and a 25% reduction in diffusion.²⁹ However, there are only a few studies that have been done on the 3D reconstructed microstructure of ASSBs.^{10,11,30,31} Li et al. reconstructed the real 3D geometry of an ASSB using synchrotron transmission X-ray microscopy tomography.¹¹ They showed that particle-based ASSBs have a critical SE/AM interfacial issue that highly influences the lithium-ion transport and intercalation reaction rate, causing low capacity, poor rate capability, and cycle life.¹¹ Tippens et al. used in situ CT to investigate the SE/lithium metal electrode interface during cycling.³⁰ They demonstrated that fracture formation is the main reason for the impedance increase during cycling.³⁰ Choi et al. reconstructed an ASSB composite cathode with FIB-SEM to analyze its physical properties including volume ratio, connectivity, tortuosity, and pore formation.¹⁰ Later, they analyzed the electrochemical lithiation/delithiation inside ASSB composite cathodes with 3D atom-probe tomography,³¹ showing that poor SE/AM contact triggers significant lithium-ion variation during lithiation/delithiation.³¹

Overall, inadequate fundamental understanding and quantitative insights on the SE/AM interface is one of the main challenges that

hinders further development of ASSBs.³ 3D reconstructed microstructures can be used as the model geometry along with a multi-physics modeling framework to provide quantitative insights about the mechanical and electrochemical behavior of ASSBs. To the best of the authors' knowledge, there is no multi-physics model developed for ASSBs based on the 3D reconstructed electrode. In the presented study, a multi-physics model is developed for ASSBs based on the reconstructed 3D morphology of electrodes for an ASSB. The model includes charge transfer kinetics at the SE/AM interface, diffusion and migration in the SE, and diffusion in the AM in the reconstructed 3D morphology of the three-phase electrode. The model is then employed to investigate the effect of compression on the ASSB behavior. In this way, the model is simulated for two different reconstructed geometries, obtained from electrodes fabricated under two different pressing pressures. This paper is structured in the following fashion: first, the electrode fabrication, synchrotron transmission X-ray microscopy (TXM) imaging techniques, and three-phase electrode reconstruction are discussed. The ASSB was processed and reconstructed by the AvizoTM software package. Then, the modeling steps, morphological analysis, governing equations, and geometry selection are presented. The 3D modeling framework is implemented in Comsol Multiphysics 5.4. Finally, the simulation results are shown and discussed with concluding remarks.

Experimental

Material synthesis and electrode fabrication.— $\text{Li}_{1.3}\text{Ti}_{1.7}\text{Al}_0.3(\text{PO}_4)_3$ (LTAP) was synthesized using aluminum oxide (Al_2O_3), titanium dioxide (TiO_2), lithium carbonate (Li_2CO_3), and ammonium dihydrogen phosphate ($(\text{NH}_4)_2\text{H}_2\text{PO}_4$). The solid mixture was ground and heated, then ball milled for 6 h, reheated for 2 h, and again ball milled for 12 h to obtain the final LTAP powder. The all-solid-state electrode is fabricated using $\text{Li}(\text{Ni}_{1/3}\text{Mn}_{1/3}\text{Co}_{1/3})\text{O}_2$ (NMC) as the AM, Super-P carbon as the electron conductor, and LTAP as the SE with a mass ratio of 47:6:47 (wt%). Then, the electrode was pressed under two different pressing pressures (700 psi and 1300 psi) to modify the porosity and interfacial contact of the SE and AM. The synthesis method and fabrication steps are detailed in our previous papers.^{11,32}

TXM tomography.—TXM within the Advanced Photon Source (APS) facility at Argonne National Laboratory was employed to obtain the morphological data of the three-phase electrode. A 8 keV beam was utilized to capture the images by rotating the sample for 180° with 2 s exposure time at each rotational step increment (0.25°). A total of 1000 virtual 2D slices were reconstructed. The 3D reconstructed volume was $700 \times 700 \times 1000$ voxels with $58.2 \times 58.2 \times 58.2 \text{ nm}^3$ voxels resolution. The electrodes were fabricated and imaged at two pressing pressures, where external pressing pressure directly affects the physical properties of the electrode. Figures 1a–1c shows the representative 2D slice images of the electrode fabricated under 700 psi and 1300 psi pressure, respectively. The white domain represents the AM, the gray is the SE and the black domain is the void space. AvizoTM was used for the segmentation of AM, SE, void spaces, and reconstruction of the three-phase electrode. The precisions of volume fractions are highly depending on the threshold selection. Therefore, to reduce the noise of images, a median filter was applied. This filter is an effective way to remove impulse noises. Then, a de-blur filter was used to increase the contrast between phases. The two thresholds were chosen manually since the 3 phases are clearly distinguishable. Segmentation with two thresholds, one separating the pore and SE phases and the other separating the AM and SE causes the formation of a thin layer of SE at the SE/AM interface. This very thin layer of SE is due to the grayscale gradient and is not realistic. Therefore, a dilation algorithm was used to replace the SE thin layer with the extension of the AM which has less than 5 pixels thickness and causes negligible error owing to the comparatively large size of the

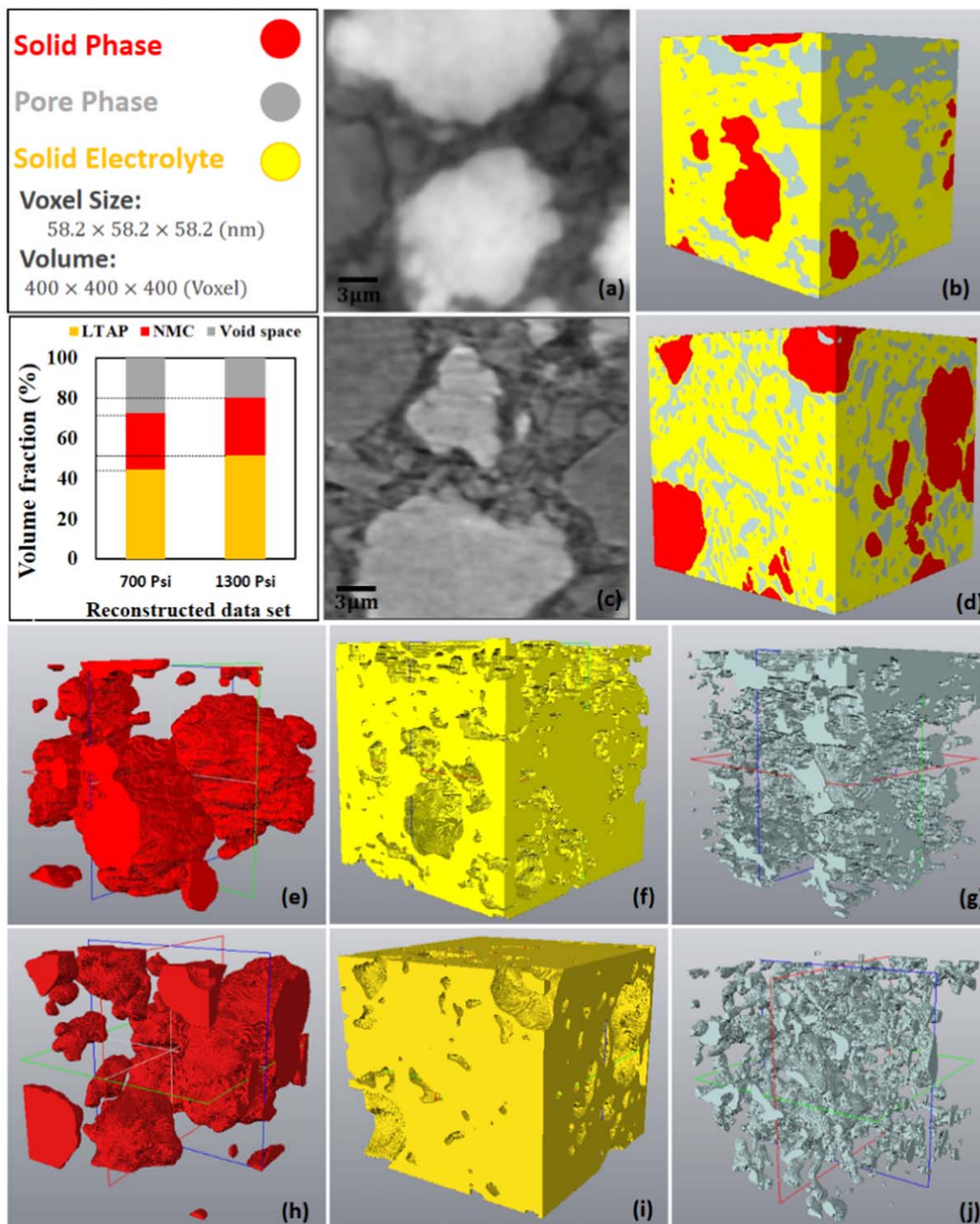


Figure 1. 2D CT images of the electrode at two pressing pressures, (a) 700 psi and (c) 1300 psi. 3D reconstructed morphology of the electrode at two pressing pressures, (b) 700 psi, and (d) 1300 psi. (e) AM, (f) SE, and (g) void space at 700 psi. (h) AM, (i) SE, and (j) void space at 1300 psi.

AM particles. The thresholds were precisely chosen and manually checked over the 2D images to ensure that the final reconstructed 3D geometry is within an acceptable error. In fact, the size of pixels (58.2 nm) is very smaller than most of the particles which highly decrease the error. The same thresholds were used for both pressing pressures. Finally, the 3D morphologies of the three-phase electrode was reconstructed after dilation. Figures 1e–1g represents the AM phase, SE, and void space resulting from 700 psi pressure and Figs. 1h–1j represents the same phases after 1300 psi pressure. Super-P carbon volume fraction is included in the void phase. Figure 1 shows that as the pressing pressure increases, the volume

fraction of the AM and SE is increased while the fraction of void space is decreased. Later, the effect of external pressing pressure on the electrode physical properties and void space volume fraction will be thoroughly discussed.

Modeling

Morphological and transport properties.—3D reconstructed microstructures of the three-phase electrode at two pressing pressures were analyzed to obtain its physical properties including electrode porosity, ϵ , volume specific surface area, a , and directional

tortuosity, τ . Tortuosity is defined as the free-space transport decrease caused by the electrode geometry and complex ion pathway. The transport problem has a direct analytical solution for simple geometries, or finite element/finite difference methods are used for complex geometries.³³ Tortuosity is defined as

$$\tau = \varepsilon\sigma / \sigma_{eff}, \quad [1]$$

where σ is the bulk ionic conductivity in the SE and σ_{eff} is the effective ionic conductivity. To obtain directional tortuosity, a FEM simulation of potential distribution, φ , using Laplace equation is performed on the SE domain:

$$\nabla \cdot (\nabla \varphi) = 0, \quad [2]$$

To obtain the directional tortuosity of the SE for electrodes fabricated under two pressures (Figs. 1g and 1j), the potential of two parallel faces (inlet/outlet) is set to 0 and 1 and the rest of the faces are set to zero flux. Then, J , the areal flux at the inlet/outlet can be calculated based on integration over the inlet/outlet boundary (S) by:

$$J = \int_S \sigma \frac{\partial \varphi}{\partial x_i} ds. \quad [3]$$

and σ_{eff} is calculated by:

$$\sigma_{eff} = \frac{J L}{A \Delta \varphi}, \quad [4]$$

where A is the perpendicular cross-section area, L is the distance between inlet and outlet, and $\Delta \varphi$ is the potential difference, which is set to 1. If we substitute Eqs. 3 and 4 into 1, the directional tortuosity can be calculated by:

$$\tau_i = \frac{\varepsilon A}{L \int_S \frac{\partial \varphi}{\partial x_i}}. \quad [5]$$

Equation 5 shows that directional tortuosity is not a function of the domain ionic conductivity.

The Bruggeman correlation is widely used in various fields³³ to estimate the tortuosity of porous media; it estimates τ as a function of porosity³⁴ by:

$$\tau = \varepsilon^{-0.5} \quad [6]$$

This correlation is based on solving the diffusive transport problem by considering either spheres or cylinders as transport obstructions. However, the accuracy of the Bruggeman relation has been questioned for complex microstructures.³³ To be able to

compare the directional tortuosities obtained from the reconstructed geometries by the Bruggeman tortuosity, the characteristic tortuosity is suggested based on directional tortuosities by³⁵:

$$\tau_c = 3[\tau_x^{-1} + \tau_y^{-1} + \tau_z^{-1}]^{-1} \quad [7]$$

Where τ_x, τ_y, τ_z are directional tortuosities obtained by Eq. 5.

Governing equations.—The model governing equations include the charge transfer kinetics at the SE/AM interface, diffusion and migration of ions in the SE, and diffusion of ions in the AM. The equations consist of five unknown variables c_{Li} , c_{Li^+} , c_{n^-} , φ_S , and φ_{SE} which represent lithium concentration in the AM, lithium-ion concentration in the SE, negative charge concentration in the SE, AM potential, and SE potential, respectively; these are determined by solving mass and charge transport equations in the AM and SE domains and considering the electro-neutrality condition in the SE (Fig. 2). The equations are implemented on the three-phase reconstructed structure of the ASSB to obtain the electrochemical property distributions in the real microstructure as well as the voltage profiles. As mentioned previously, in ASSBs the SE facilitates ion conduction. The ionic conductivity of the SE is generally several orders of magnitude lower than common liquid electrolytes.³⁶ Therefore, it is assumed that all electrochemical reactions occur at the SE/AM interface.¹³ Fick's mass transport law is used to describe the lithium diffusion in the AM domain as^{24,37}:

$$J_{Li} = -D_{Li} \nabla c_{Li}, \quad [8]$$

$$\frac{\partial c_{Li}}{\partial t} = -\nabla \cdot J_{Li}, \quad [9]$$

Where D_{Li} , J_{Li} , c_{Li} are the diffusion coefficient of lithium, lithium flux, and lithium concentration in AM, respectively. On the SE/AM interface, the reaction is described using Butler–Volmer kinetics:

$$i_{pos} = i_{0, pos} \left(e^{\frac{\alpha_{pos} F \eta}{RT}} - e^{-\frac{(1-\alpha_{pos}) F \eta}{RT}} \right), \quad [10]$$

$$i_{0, pos} = F k_{pos} \left(\frac{(c_{Li, max} - c_{Li}) c_{Li^+}}{(c_{Li, max} - c_{Li}) c_{Li^+, 0}} \right)^{\alpha_{pos}} \left(\frac{c_{Li} - c_{Li, min}}{c_{Li, max} - c_{Li, min}} \right)^{1-\alpha_{pos}} \quad [11]$$

where $c_{Li, max}$ and $c_{Li, min}$ are the maximum and minimum of the lithium concentration in AM, and i_{pos} , $i_{0, pos}$, k_{pos} , α_{pos} , and F are the current density, exchange current density, the reaction rate constant, apparent transfer coefficient, and Faraday's constant, respectively.

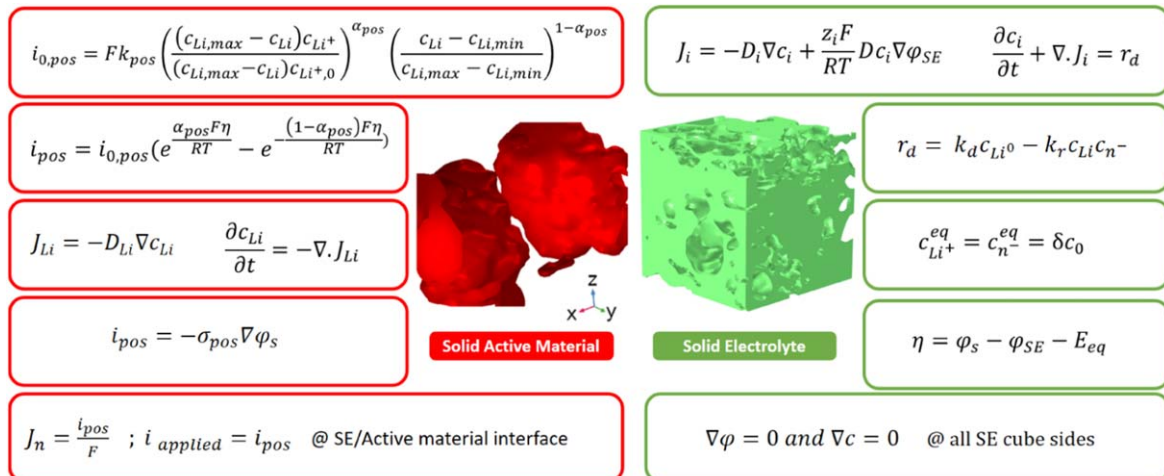


Figure 2. Modeling framework.

The AM potential can be calculated by:

$$i_{pos} = -\sigma_{pos} \nabla \varphi_s, \quad [12]$$

where E_{eq} is the open circuit potential, and φ_{SE} , φ_s , and σ_{pos} are the SE potential, AM potential, and conductivity of solid active material, respectively. In the SE, the chemical reaction is:



where bonded lithium (Li^0) is transferred to a lithium ion and releases a negative charge.¹³ k_d is defined as the dissociation rate of this reaction and the inverse reaction rate is defined as k_r . Therefore, the overall reaction is¹³:

$$r_d = k_d c_{Li^0} - k_r c_{Li^+} c_{n^-}, \quad [14]$$

$$c_{Li^+}^{eq} = c_{n^-}^{eq} = \delta c_0, \quad [15]$$

where δ is the fraction of the total dissociated lithium at equilibrium and $c_{Li^+}^{eq}$, $c_{n^-}^{eq}$, and c_0 are the lithium-ion concentration at equilibrium, negative charge concentration at equilibrium, and total lithium concentration in the SE, respectively. Transport of lithium ions and negative charges in the SE are modeled by the Nernst-Planck equation¹⁵:

$$\frac{\partial c_i}{\partial t} + \nabla \cdot J_i = r_d, \quad [16]$$

$$J_i = -D_i \nabla c_i + \frac{z_i F}{RT} D_i c_i \nabla \varphi_{SE}, \quad [17]$$

where z_i and D_i are the species' charge and diffusivity, respectively. The electro-neutrality condition implies that, at any time in the SE, $c_{Li^+} = c_{n^-}$. Faraday's law is used to couple the flux at the interface of the SE and AM as:

$$J_n = \frac{i_{pos}}{F}, \quad [18]$$

where n is the normal unit vector to the interface and J_n is the lithium mass transport flux at the SE/AM interface. At all SE cube sides, $\nabla \varphi = 0$ and $\nabla c = 0$.

Each of the transport processes has a contribution to the total overpotential.³⁸ The concentration overpotential in AM is¹³:

$$\eta_c = \varphi_{pos} - \varphi_{pos}^{eq}, \quad [19]$$

where φ_{pos} and φ_{pos}^{eq} are the AM potential and potential at equilibrium. Kinetic overpotential at the SE/AM and Ohmic overpotential in SE are derived by³⁸:

$$\eta_k = \frac{1}{A_{interface}} \int \eta_{Butler-Volmer} dA_{interface} \quad [20]$$

$$\eta_r = \Delta \varphi_{SE} \quad [21]$$

where $A_{interface}$ is the SE and AM interface area and φ_{SE} is the SE potential.

RVE selection.—It should be noted that using the whole 3D reconstructed electrode morphology as the model geometry would be computationally expensive. One way to address this issue is to use a representative volume element (RVE) instead of the whole electrode structure. RVE is a sub-volume of the whole electrode that has the same measured property values compared to the whole electrode with negligible error.³⁹ The SE, AM, and pore volume fractions and volume specific surface area of the AM are calculated to figure out the size of RVE. The three-phase volume fractions for the whole domains with seven different volume sizes are presented in Table I for two pressing pressures. Table I shows that the SE, AM, and pore volume fractions for an RVE size of 7097 μm^3 and larger are similar to the whole electrode (within 2% error). Accordingly, the smallest suitable RVE size would be 7097 μm^3 ; however, to minimize the error of selecting a specific region of the geometry, the electrochemical performance simulation and morphological analysis were modeled on a sub-volume geometry with the dimension of 400 × 400 × 400 Voxels (12617 μm^3) (Fig. 3), i.e., all represented 3D morphologies in Figs. 6–13 have 400 × 400 × 400 voxels; current density direction and current collector illustrated in Fig. 3c.

Results and Discussion

To investigate the heterogeneity and isotropy of the electrode's microstructure, tortuosities of the SE domain were estimated and compared in different directions using the method presented in the modeling section. The directional, characteristic, and Bruggeman tortuosities are presented in Table II. The characteristic tortuosity, τ_c , is obtained using Eq. 7 and the Bruggeman tortuosity is calculated with Eq. 6 where ε is equal to the SE volume fraction. The Bruggeman tortuosity, obtained based on a geometry of equally sized spheres, is slightly lower than the characteristic tortuosity due to its neglecting of the heterogeneous structure. Furthermore, lower tortuosity of the electrode with higher pressing pressure verifies that higher pressing pressure leads to less void space and consequently less ionic transport resistance through the SE; i.e., in this case higher pressing pressure causes 26.8% less void space in the electrode and consequently 11.1% less tortuosity and 36.9% higher volume specific surface area.

Although 1D models^{13,14} can predict the voltage-capacity performance by considering macroscale geometry, they fail to describe the variation of physical and electrochemical properties inside the heterogeneous electrode structure. To obtain the spatial distribution

Table I. The volume fraction of different phases of the reconstructed 3D geometry at two pressing pressures.

	Pressing pressure 700 psi						
Total Volume (μm^3)	19714	15968	12617	9660	7097	4929	3154
Volume specific surface area ($1/\mu\text{m}$)	0.522	0.531	0.554	0.562	0.583	0.593	0.612
Solid Active material (%)	28.1	27.6	27.9	29.3	29.2	27.1	27.2
Solid Electrolyte (%)	44.9	45.1	44.5	43.2	43.3	57.6	60.5
Pore (%)	27.0	27.3	27.6	27.5	27.5	15.3	12.3
	Pressing pressure 1300 psi						
Total Volume (μm^3)	19714	15968	12617	9660	7097	4929	3154
Volume specific surface area ($1/\mu\text{m}$)	0.617	0.622	0.631	0.642	0.648	0.652	0.664
Solid Active material (%)	28.1	27.8	28.7	27.7	28.2	27.4	19.3
Solid Electrolyte (%)	52.6	53.2	51.5	53.8	53.1	55.1	60.6
Pore (%)	19.3	20.0	19.8	18.5	18.7	17.6	20.1

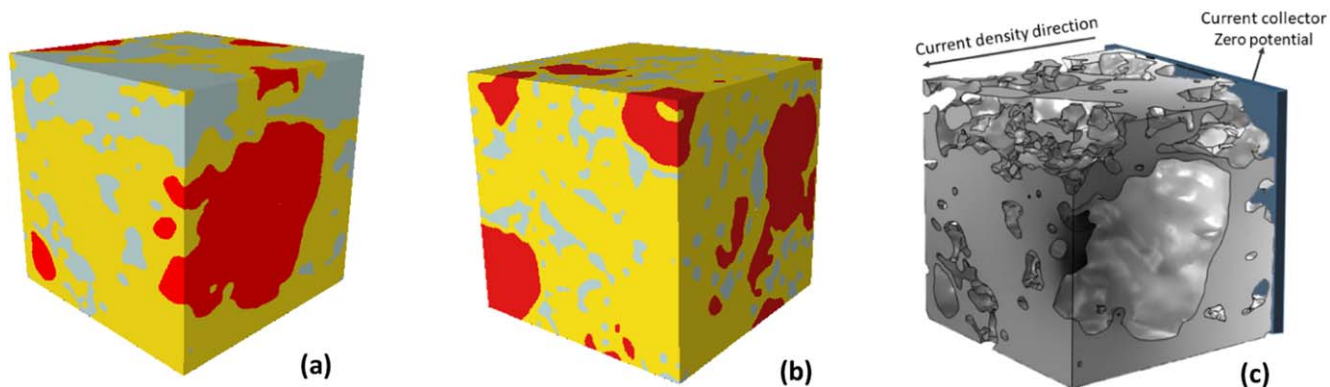


Figure 3. 3D reconstructed RVEs of the ASSB at (a) 700 psi, and (b) 1300 psi pressing pressure; yellow, red, and grey colors represent the SE, AM, and void space, respectively, and (c) current collector and current density direction.

Table II. Directional tortuosities based on 3D reconstructed geometry and implementing heat transport analogy.

	700 psi	1300 psi
In-plane directional tortuosity, τ_x	1.53	1.52
In-plane directional tortuosity, τ_y	1.54	1.40
Through-plane directional tortuosity, τ_z	1.8	1.38
Characteristic tortuosity, τ_c	1.61	1.43
Bruggeman tortuosity, τ_B	1.50	1.39

of physical and electrochemical properties inside the electrode microstructure including lithium concentration, current density, and potential, the presented model in the modeling section is simulated on the 3D reconstructed electrode structures (Fig. 3). Moreover, to investigate the effect of the external pressing pressure on the physical and electrochemical phenomena, the electrode structures fabricated under two pressures of 700 and 1300 psi are considered.

To validate the accuracy of the developed model, the simulation results are compared against the experimental cycling performance of an ASSB with LTAP as SE and LiMn_2O_4 as AM for which experimental performance data was available.³² Figure 4a shows the modeling performance against the experimental data for galvanostatic charging at 0.1 C current rate. The model/experiment comparison shows relatively good agreement. Table III shows the

parameters used to simulate the modeling result in Fig. 4. D_{Li} , the diffusion coefficient for lithium in the AM, D_{Li^+} , the diffusion coefficient for lithium ions in the SE, and D_{n^-} , the diffusion coefficient for n^- in the SE are considered the model adjustable parameters and determined to be $1.76 \times 10^{-13} \text{ m}^2 \text{ s}^{-1}$, $0.9 \times 10^{-13} \text{ m}^2 \text{ s}^{-1}$, and $5.1 \times 10^{-13} \text{ m}^2 \text{ s}^{-1}$, respectively, by comparing the simulation results against the experimental data by visual fit. The considered diffusion coefficient values in the presented model are in the range of reported values in literature (10^{-16} – $10^{-12} \text{ m}^2 \text{ s}^{-1}$).^{36,40,41} Additionally, to verify the validity of the developed 3D model, the discharge performance is compared with the available 1D model¹³ using the same model parameters presented in Table III. In order to scale the volumetric current source term for the 1D model, $i_{1D} = \frac{a}{a_0} i_{3D}$, where a is the volume specific area obtained by reconstructed morphology (Table I) and a_0 is the volume specific area for the 1D model. At various current rates, 3D and 1D models have almost identical voltage profiles; however, the 3D model predicts slightly higher ohmic resistance due to included electrode microstructure in the model geometry (Fig. 4b).

After validating the developed model, the model is employed to predict the galvanostatic discharge performance of the ASSB with NMC as the active material. To demonstrate the effect of different pressing pressures during electrode fabrication on the ASSB behaviors, the simulation results are conducted on the reconstructed RVEs with two pressing pressures, (Fig. 3 and Supplementary Video 1 is available online at stacks.iop.org/JES/167/100558/mmedia). Applying external pressing pressure causes lower void space volume fraction and leads to

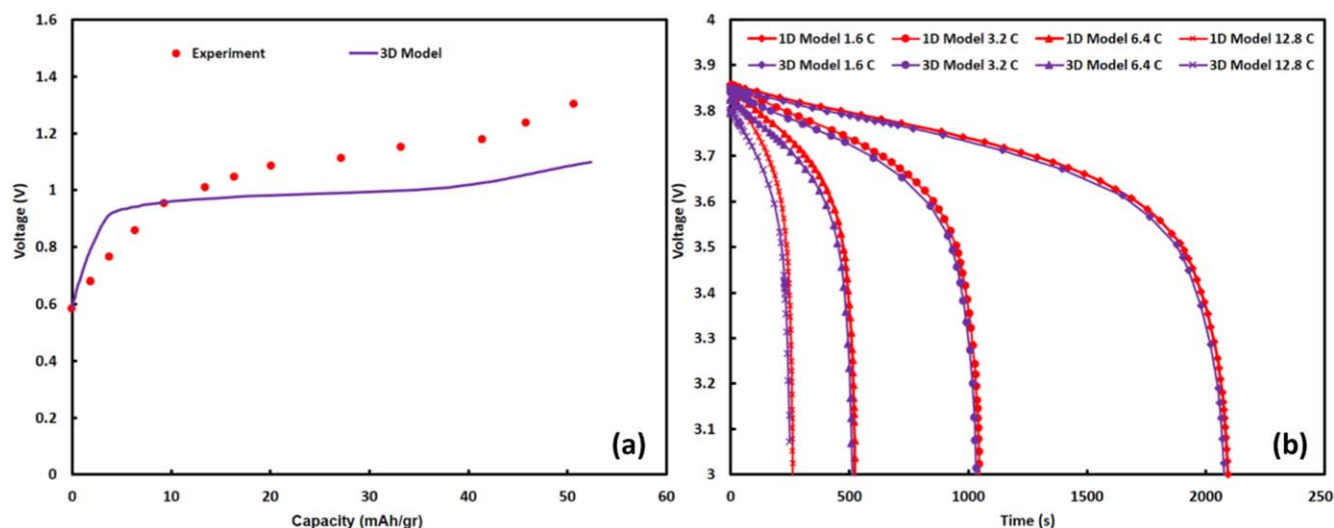


Figure 4. (a) Comparison of the modeling (line) and experimental data set (dots), and (b) comparison of the 3D developed model with 1D Model based on Ref. 13.

Table III. Model parameters.

Parameter	Unit	Estimated value	Description
a_0	mol m^{-3}	6.01×10^4 ¹³	Total activity of Li atoms in SE matrix
k_r	$\text{m}^3 \text{mol}^{-1} \text{s}^{-1}$	0.9×10^{-8} ¹³	Lithium-ion recombination reaction rate
δ	—	0.18 ¹³	Fraction of free lithium-ion in equilibrium
D_{Li^+}	$\text{m}^2 \text{s}^{-1}$	0.9×10^{-13}	Diffusion coefficient for lithium-ion in the SE (LTAP)
D_{Li}	$\text{m}^2 \text{s}^{-1}$	1.76×10^{-13}	Diffusion coefficient for lithium in AM (NMC)
D_{n^-}	$\text{m}^2 \text{s}^{-1}$	5.1×10^{-13}	Diffusion coefficient for n^- in the electrolyte
a_{pos}^{max}	mol m^{-3}	2.33×10^4 ¹³	Maximum activity of the lithium in the positive electrode
α_{pos}	—	0.6 ¹³	Charge transfer coefficient in the positive electrode
k_{poa}	$\text{mol m}^{-2} \text{s}^{-1}$	5.1×10^{-6} ¹³	Rate constant charge transfer positive electrode
L	μm	14.33	Thickness of the SE (for 1D model)
M	μm	8.95	Thickness of the AM (for 1D model)

more homogenous distribution of electrochemical properties. Although the high external pressure would increase the contact area between the SE and active materials by decreasing the void space fraction, it can damage the SE due to its brittle nature.⁴² However, the capacity of the cell with different pressing pressures is almost the same at various c-rates (Fig. 5a); Fig. 5a shows that there is a higher ohmic loss at lower pressing pressure that could be attributed to poor SE/AM contact and higher interfacial resistance. Figure 5b illustrates the contribution of the various overpotential components during discharging at 3.2 C and 12.8 C for the electrode with a 700 psi pressing pressure. It is remarkable that concentration overpotential within the AM has the largest contribution at the end of discharge due to the steep concentration gradient of lithium. During the discharge, Ohmic overpotential in SE has a considerable contribution; whereas, imperfect SE/AM interface leads to a large kinetic overpotential at the beginning of the discharge process. On the other hand, at high discharge current rate (12.8 C), the kinetic overpotential contribution becomes larger and ohmic overpotential contribution is less than 3.2 C discharge rate.

1D models are based on macro-sized geometries (a 1D line) and do not consider the effect of microstructure on the electrochemical property distribution.^{12,13,15} However, these assumptions are not valid for real ASSB cells, which have an inhomogeneous microstructure with AM particles of different sizes and shapes and random void space formations. Even though the 1D models can successfully predict the capacity performance, they fail to predict the physical and electrochemical property variations which may cause cell

degradation.^{38,43} The key advantage of using reconstructed morphologies in this study is to visualize the heterogeneities inside the SE and AM which can contribute to electrode degradation. In fact, stress can be much higher around the concave regions within the electrode's microstructure due to local high lithium concentration which can initiate mechanical failures^{23,44}; while a macro-homogenous model cannot capture the in-homogeneities. The presented study sheds light on the spatial distribution of electrochemical properties in ASSBs and specifically the effects of pressing pressure on the cell performance and physical and electrochemical behaviors of the cell.

Figures 6a–6c, 6d–6f shows the lithium distribution in the AM at various state of charges (SOCs) during galvanostatic discharge at 3.2 C for two pressing pressures of 700 and 1300 psi, respectively. During discharge, the average lithium concentration in the AM is higher at higher pressing pressure which verifies that increasing pressure facilitates lithium-ion transport inside the AM. Figures 6g–6l presents lithium concentration histograms for two pressures; this demonstrates that higher pressure leads to more uniform lithium distribution inside the AM. At 0.7 SOC for 700 psi pressing pressure, there is a wider range of lithium distribution inside the AM, with lithium concentrations in the range of 14200–16200 (mol.m^{-3}) at 700 psi compared to 14400–15400 (mol.m^{-3}) at 1300 psi (Figs. 6g–6l). In addition, Figs. 6a–6f shows that smaller particles have higher lithium concentrations due to their higher specific surface areas, comparable with previous heterogeneous study with liquid electrolyte.^{22,24} The dashed lines in the Fig. 6 histograms represents the concentration value of the homogenous Danilov 1D

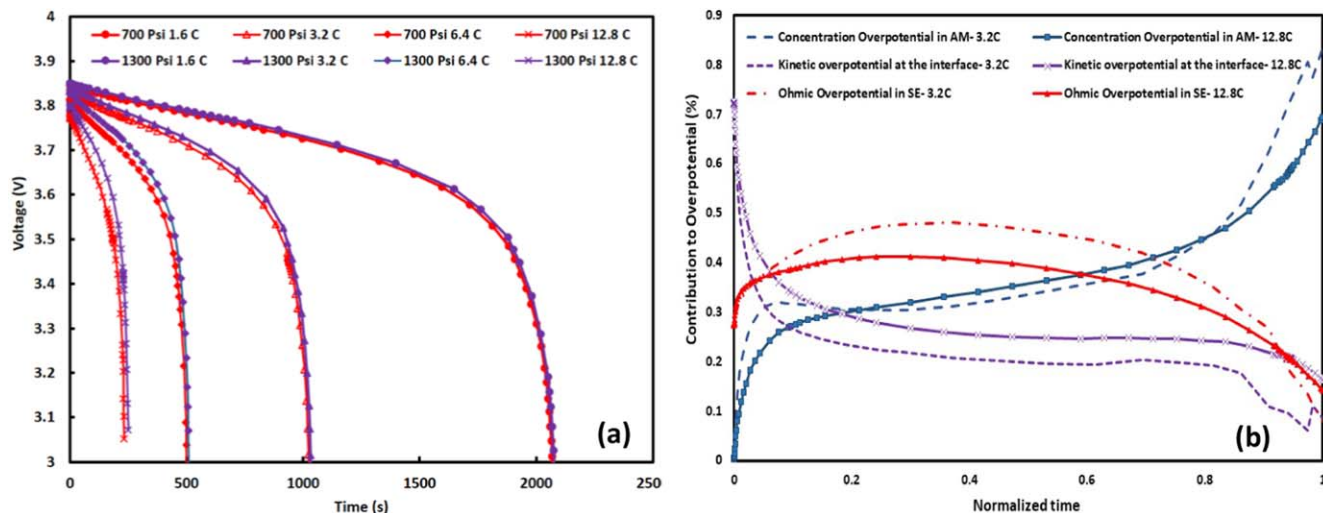


Figure 5. (a) Effect of external pressing pressure on the galvanostatic discharge performance of the ASSB at various current rates, and (b) overpotentials in the composite electrode under 700 psi pressing pressure at two current rates.

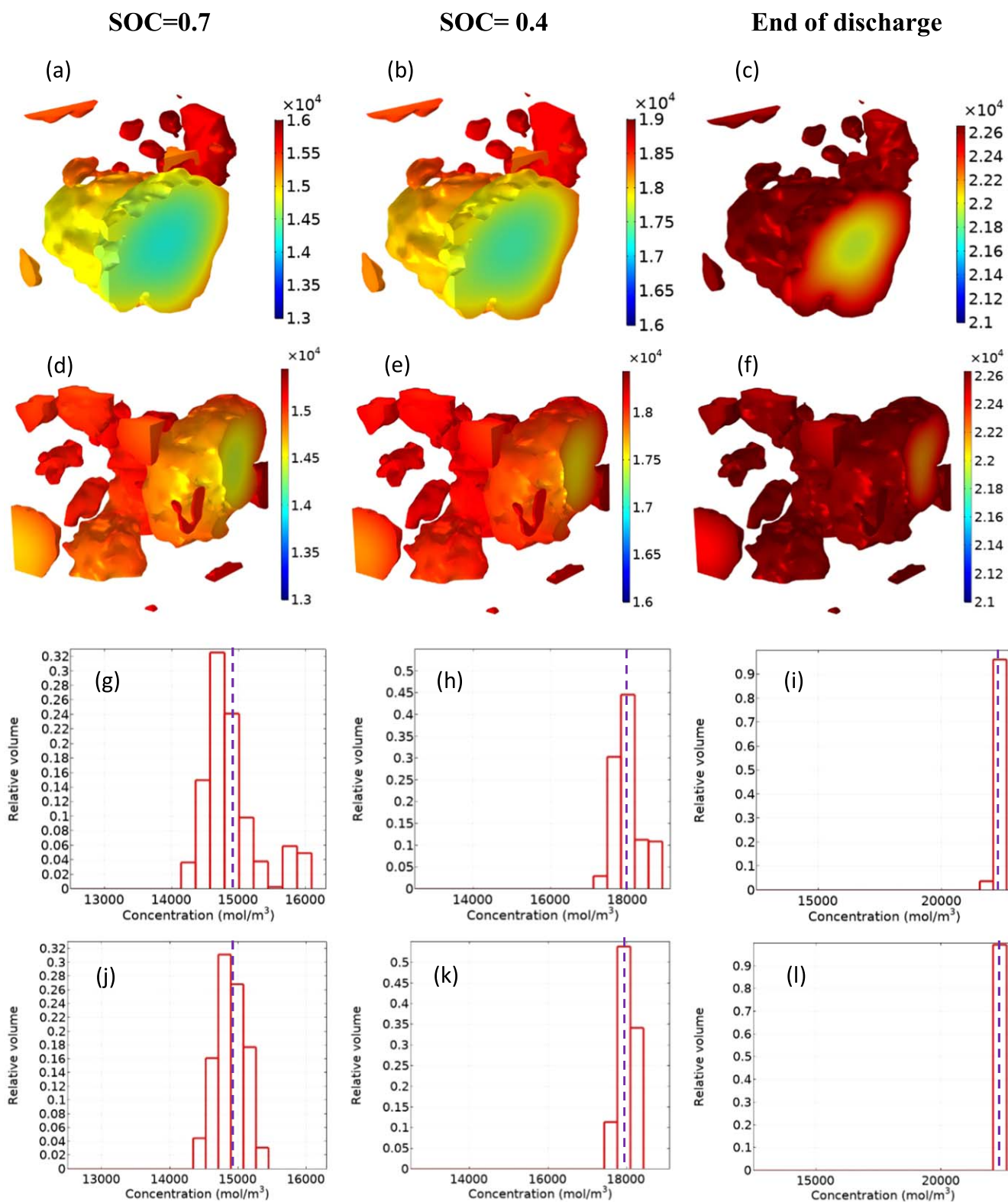


Figure 6. Lithium concentration in the AM phase with two pressing pressures: (a)–(c) 700 psi, (d)–(f) 1300 psi at 3.2 C current rate and various SOC. Histogram representing the lithium concentration in the AM with two pressing pressures: (g)–(i) 700 psi, (j)–(l) 1300 psi during galvanostatic discharge (3.2 C) at various SOC. Dashed lines represent the 1D model values.

Model.¹³ Since the homogenous model does not consider the microstructure of the electrode, it cannot predict the distribution range of lithium concentration; however, the homogenous model result is close to the average value of the lithium concentration simulated with this 3D model.

The lithium-ion distribution in the SE is presented in Fig. 7. To show the lithium-ion gradient inside the SE, the lithium-ion distribution is illustrated on two cross-section plates. There are some specific points with higher lithium ion concentration adjacent to the void spaces, since void spaces block the lithium-ion path and

cause non-uniform lithium-ion distribution (Figs. 7a–7f). A similar trend was reported in a previous ASSB microstructural study.⁴⁵ At lower pressing pressure of 700 psi, the electrode has 16% less SE and 28% more void space compared to the electrode at 1300 psi. This leads to a 56% larger range of lithium-ion distribution in the SE at 700 psi compared to 1300 psi. At 700 psi, the lithium ions

distribute in the range of 8000–15000 (mol.m⁻³) compared to the range of 9500–13000 (mol.m⁻³) at 1300 psi. This larger range of lithium-ion concentration at low pressing pressure may cause non-uniform expansion/contraction and consequently stress formation in the cell, which can cause cell performance degradation (Figs. 7g–7l). The lithium-ion concentration based on the 1D model (dashed line)

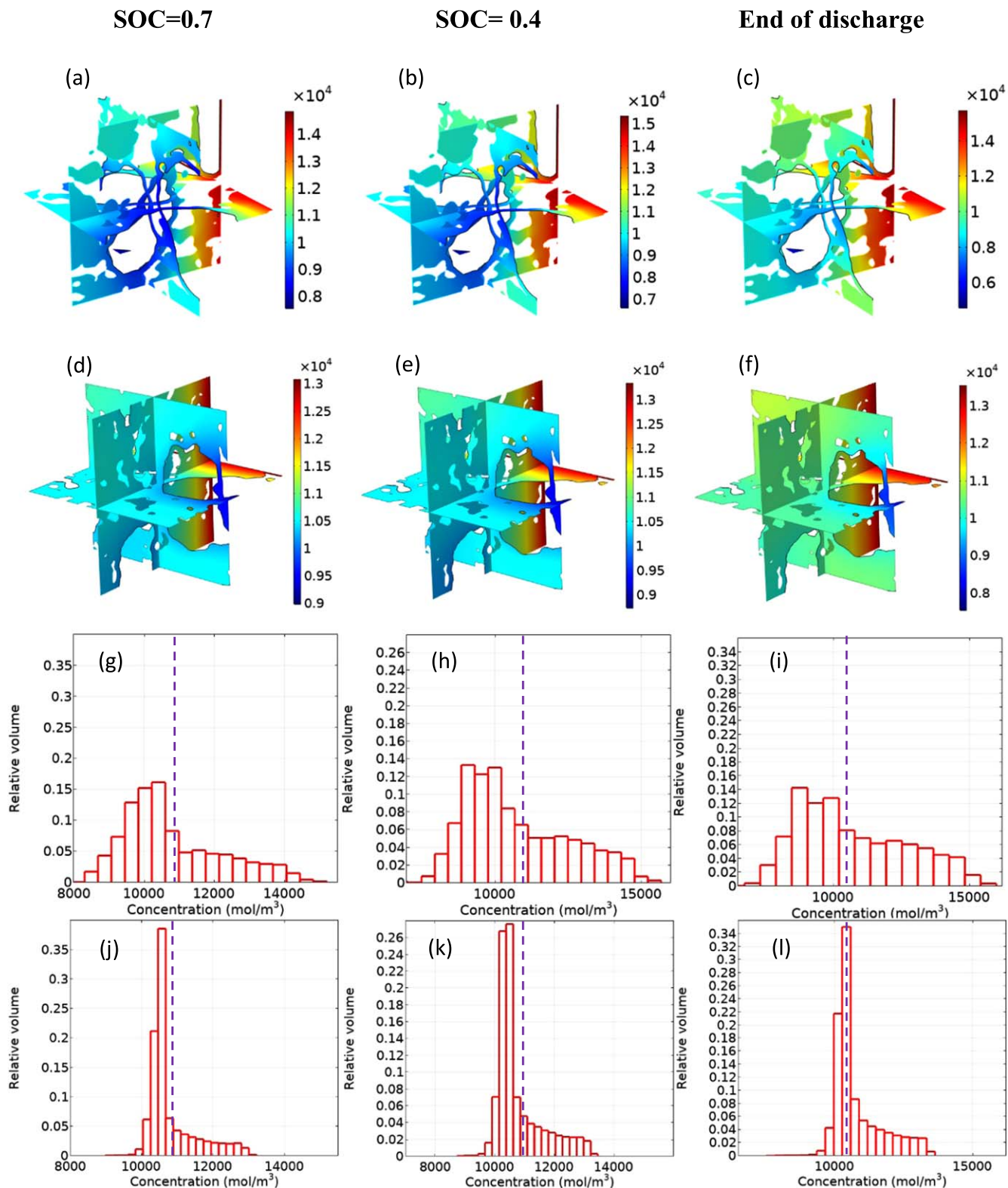


Figure 7. Lithium-ion concentration in the SE with two pressing pressures: (a)–(c) 700 psi, (d)–(f) 1300 psi at 3.2 C current rate and various SOC. Histogram representing the lithium-ion concentration with SE two pressing pressures: (g)–(i) 700 psi, (j)–(l) 1300 psi during galvanostatic discharge (3.2 C) at various SOC. Dashed lines represent the 1D model values.

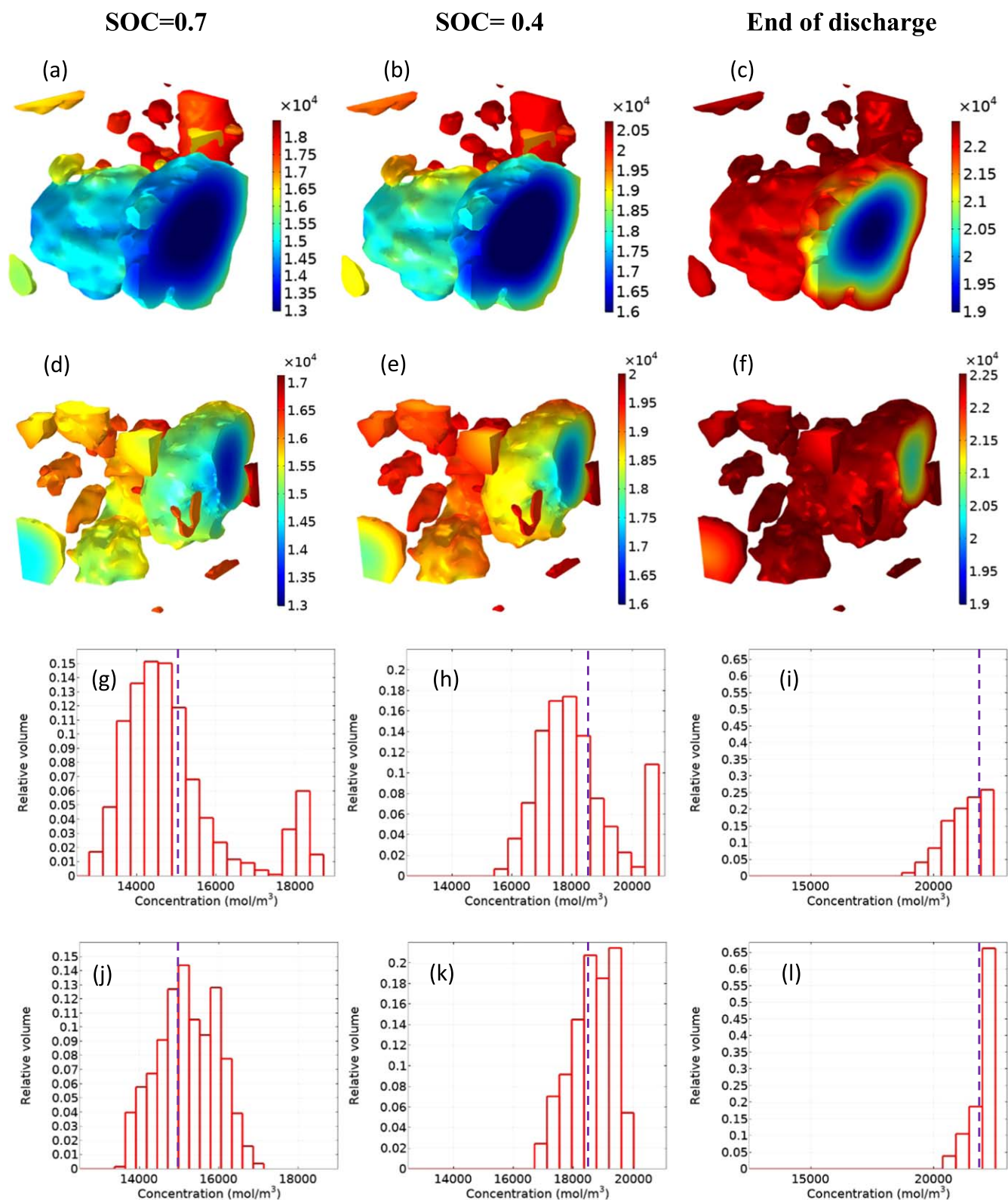


Figure 8. Lithium concentration in AM phase with two pressing pressures: (a)–(c) 700 psi, (d)–(f) 1300 psi at 12.8 C current rate and various SOC. Histogram representing the lithium concentration in AM with two pressing pressures: (g)–(i) 700 psi, (j)–(l) 1300 psi during galvanostatic discharge (12.8 C) at various SOC. Dashed lines represent the 1D model values.

is almost constant over the discharge, while lithium-ion histograms of the 3D models illustrate the variation of lithium-ion concentration during discharge.

At higher current rates, structural heterogeneity has a stronger effect on the physical and electrochemical property distributions.²⁴

To investigate the effect of pressing pressure at high currents, the lithium concentration distribution in the AM and lithium-ion distribution in the SE at 12.8 C current rate are presented in Figs. 8 and 9, respectively. Comparing Fig. 6g with Fig. 8g, it is noticeable that at the higher current rate the lithium distribution has a

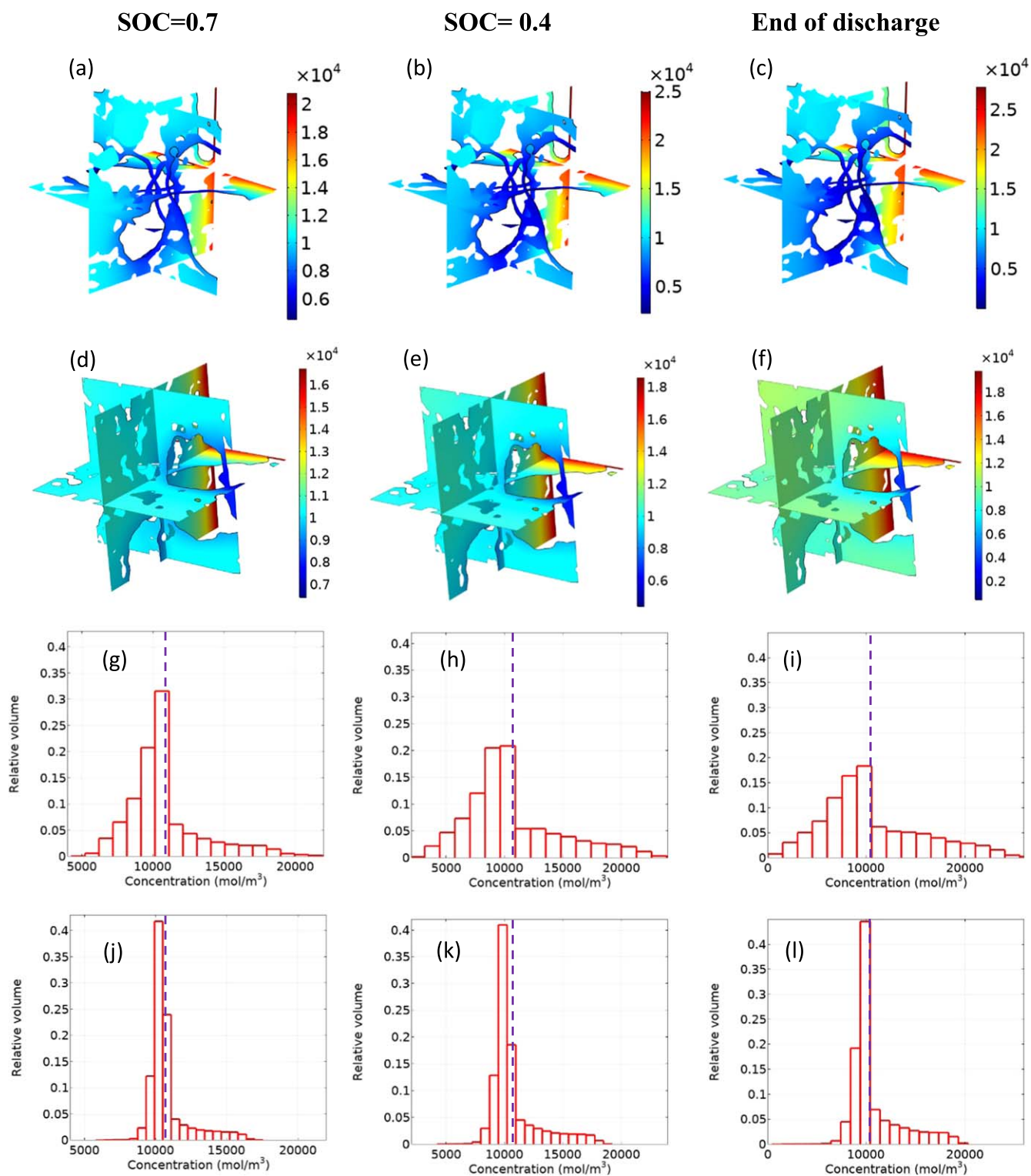


Figure 9. Lithium-ion concentration in SE with two pressing pressures: (a)–(c) 700 psi, (d)–(f) 1300 psi at 12.8 C current rate and various SOC. Histogram representing the lithium-ion concentration in SE with two pressing pressures: (g)–(i) 700 psi, (j)–(l) 1300 psi during galvanostatic discharge (12.8 C) at various SOC. Dashed lines represent the 1D model values.

240% wider range at the low pressing pressure where more void spaces and higher tortuosity causes non-uniform lithium distribution in the AM. Comparing lithium-ion distribution in the SE at 3.2 C (Fig. 7) and 12.8 C (Fig. 9), a lithium-ion concentration gradient is established along the lithium-ion transport direction and has a wider range at the higher current rates and lower pressing pressures. Additionally, at the high current rate, the lithium concentration range

highly deviates from the 1D model results (dashed line) due to the complex microstructure of the electrode which is neglected in the 1D model. It is worth noting that the range of lithium concentration within the microstructure depends on the length of the lithium diffusion path and the current rate. At high current rates, there is not enough time for lithium to fully lithiate the host active material which leads to a wider range of lithium concentration distribution.

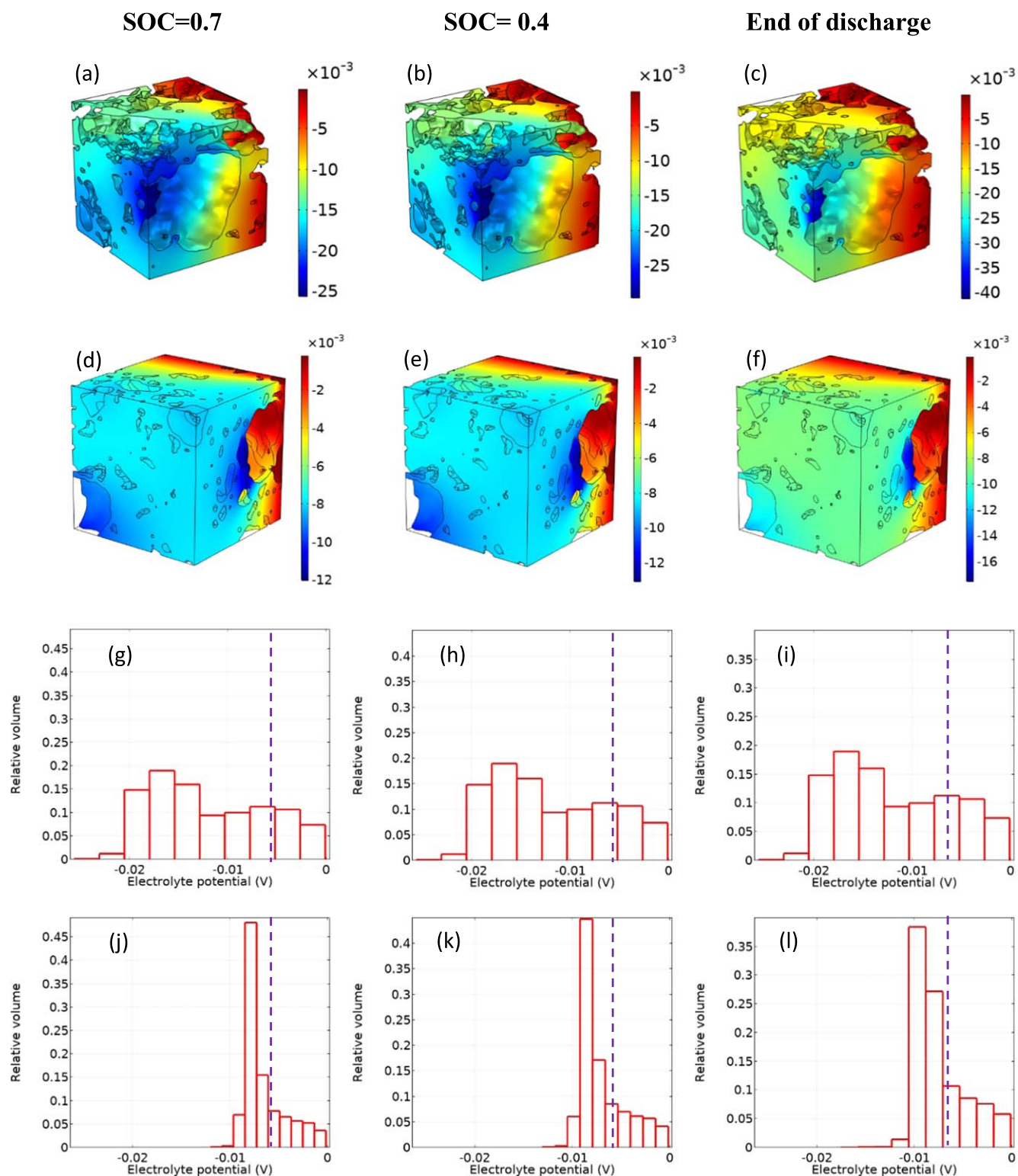


Figure 10. Potential in SE with two pressing pressures: (a)–(c) 700 psi, (d)–(f) 1300 psi at 3.2 C current rate and various SOC. Histogram representing the SE potential at two pressing pressures: (g)–(i) 700 psi, (j)–(l) 1300 psi during galvanostatic discharge (3.2 C) at various SOC. Dashed lines represent the 1D model values.

Additionally, sandglass type microstructures can cause a high local concentration gradient. Therefore, the morphology of the microstructure affects the lithium concentration distribution as well.

As mentioned, interfacial resistance and specifically void spaces hinder the lithium-ion transport.⁴⁵ To further investigate this, the SE potential and current density distribution for the two electrodes

fabricated under different pressures are presented in Figs. 10–13. Figure 10 shows that at 700 psi, the potential ranges from -40 mV to 0 mV at the end of discharge which is 2.5 times higher than the range of -16 mV to 0 mV at 1300 psi. As illustrated in Fig. 11, with increasing current rate, the electrolyte voltage drop at the end of discharge ranges from -250 mV to 0 mV which is 6.25 times higher

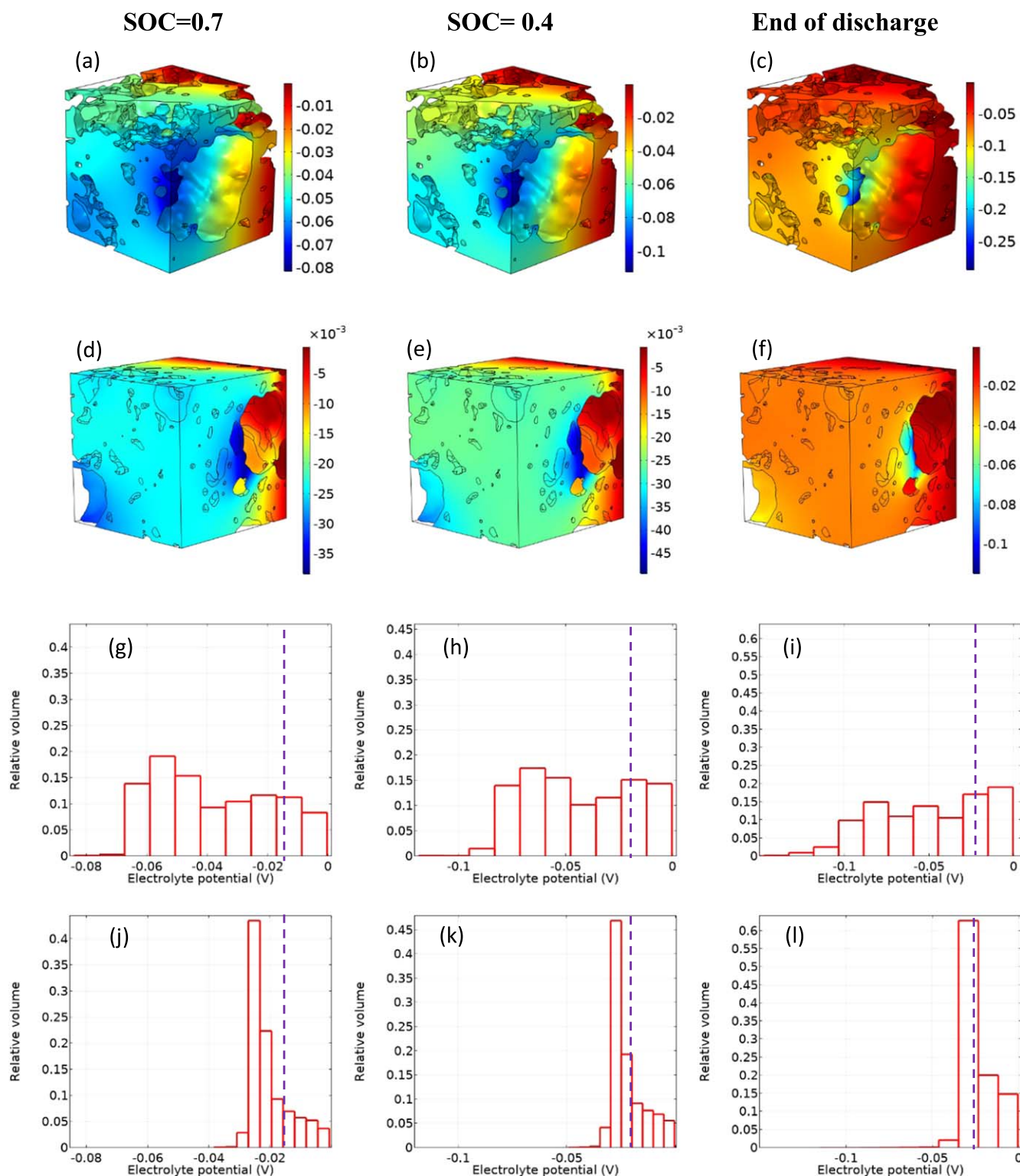


Figure 11. Potential in the SE with two pressing pressures: (a)–(c) 700 psi, (d)–(f) 1300 psi at 12.8 C current rate and various SOCs. Histogram representing the SE potential at two pressing pressures: (g)–(i) 700 psi, (j)–(l) 1300 psi during galvanostatic discharge (12.8 C) at various SOCs. Dashed lines represent the 1D model values.

compared to the voltage drop at 3.2 C; however, at higher pressing pressure increasing the current rate has less effect on the SE voltage drop. In fact, the SE voltage drop is the main contribution to the ASSBs overpotential,¹⁵ and at high current rates, it has a more significant role in determining the overpotential distribution. Chemomechanical contraction of AM during delithiation leads to contact loss and higher interfacial resistance.⁴⁶ Additionally, volume

changes during cycling may cause crack formation in SE which increases the tortuosity and lead to a capacity fade⁴⁷; however, in the presented model this effect is neglected and the aforementioned imperfect contact in the reconstructed morphologies is due to initial pore distribution in the composite electrode.

Figure 12 shows the distribution of current density at the SE/AM interface, where the complex microstructure of the electrode causes

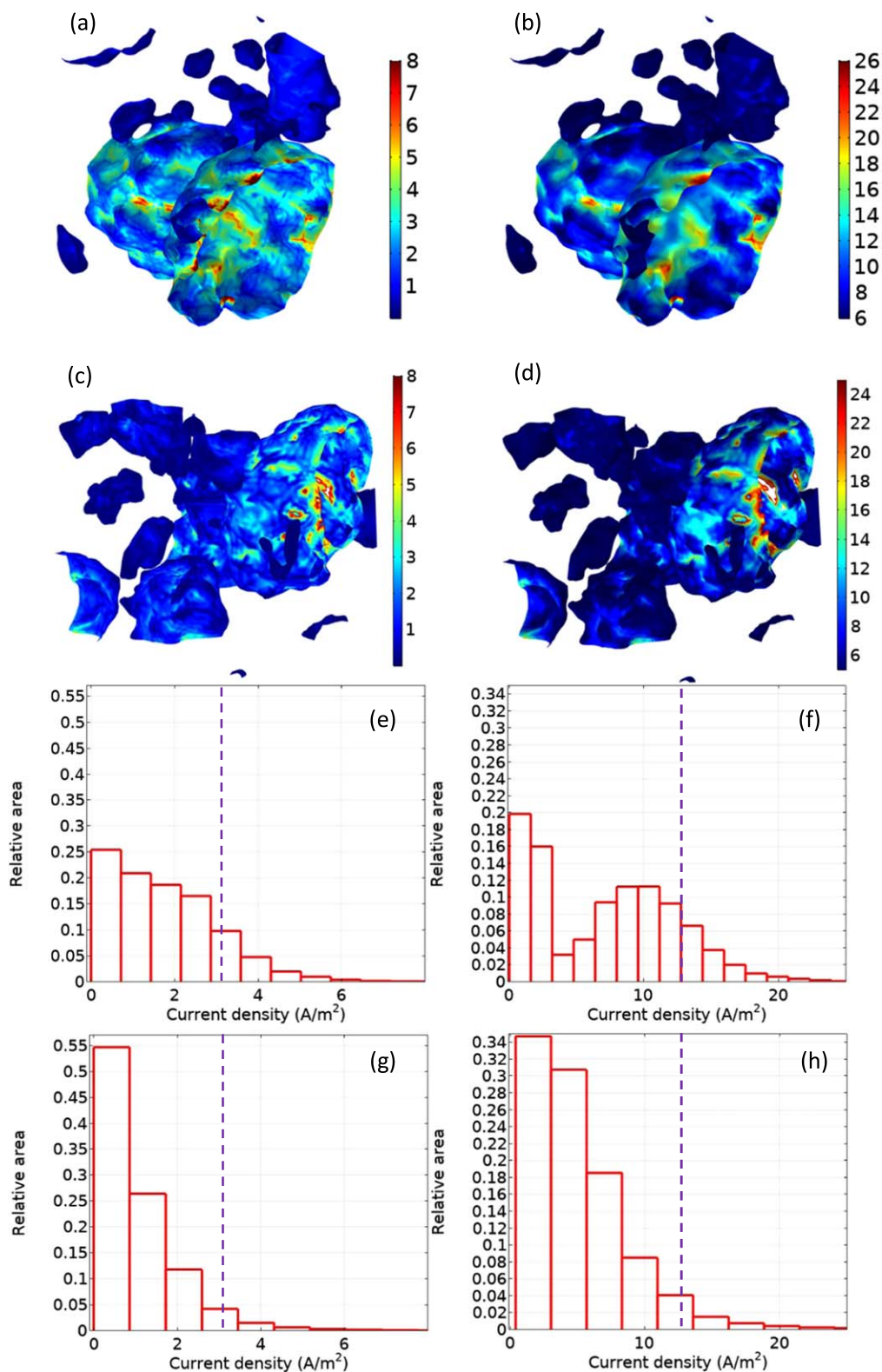


Figure 12. Current density at SE/AM interface at (a) 700 psi pressing pressure, and the end of discharge, at 3.2 C current rate, (b) 700 psi pressing pressure, and the end of discharge, at 12.8 C current rate, (c) 1300 psi pressing pressure, and the end of discharge, at 3.2 C current rate, (d) 1300 psi pressing pressure, and the end of discharge, at 12.8 C current rate. (e)–(h) Histogram representing the SE/AM interface current density at (a)–(d) conditions, respectively. Dashed lines represent the 1D model values.

large current densities within ionic pathways with a small cross-sectional area perpendicular to the current direction. At high currents, the lithium ion concentration differences in the SE and AM become larger which leads to a higher current density at the SE/AM interface.

The current density has an inhomogeneous distribution with a peak at the neck of a “sandglass” microstructure. Specifically, the current density has a wide range of distribution with several peak points with a high current density of 24 A m⁻² which is almost 2 times the

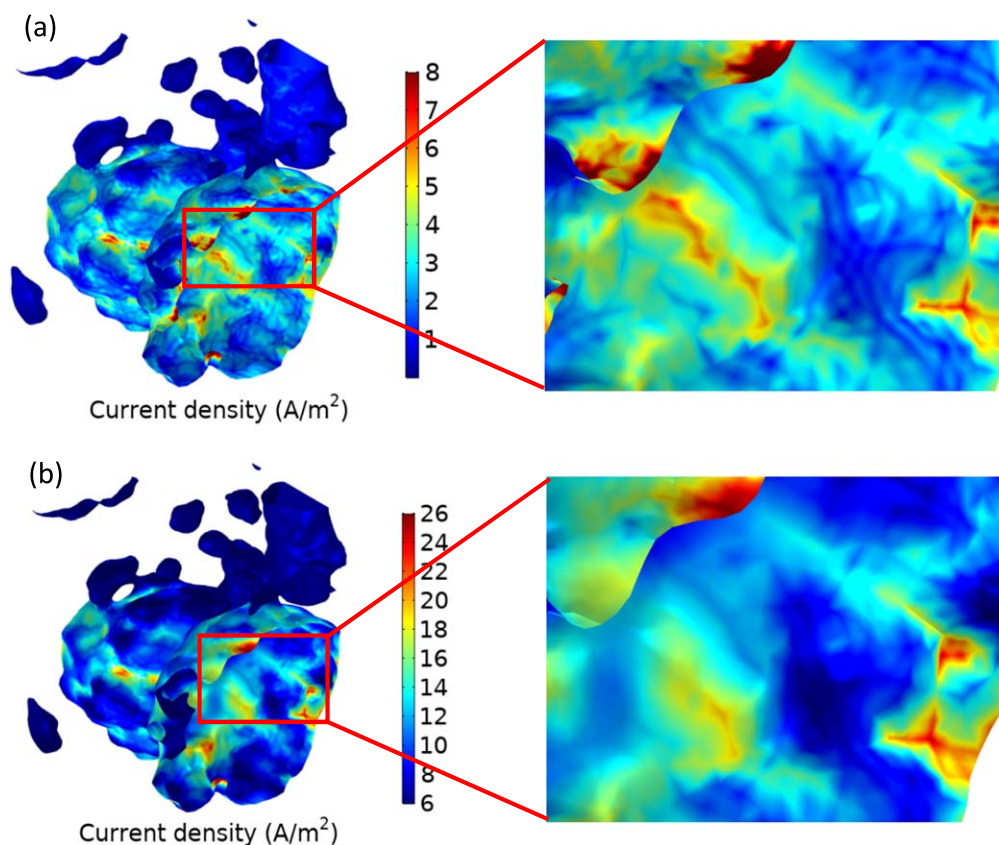


Figure 13. A close-up view of the current density distribution at the SE/AM interface at 700 psi pressing pressure, (a) 3.2 C current rate, and (b) 12.8 C current rate. The highest current density occurs near void spaces.

average current density (12.8 A m^{-2}). In the close-up view shown in Fig. 13, all of these points are observed to be located near sandglass microstructures where there is a limitation on ion transport.

Conclusions

In this study, the first 3D multi-physics simulation of ASSBs based on reconstructed X-ray CT images was accomplished. The imaging was conducted using 58.2 nm resolution synchrotron TXM for two electrodes with different external pressing pressures to investigate the effects of compression on the physical and electrochemical property behaviors. The SE's resistance to ion transport was quantified by estimating the SE tortuosity using a heat transport analogy. The simulation showed that higher pressing pressure causes 26.8% less void space in the electrode and consequently 11.1% less tortuosity and 36.9% higher volume specific surface area. Void spaces block the lithium-ion pathways in the SE and cause resistance in the electrode, which may lead to performance loss. The main advantage of the 3D heterogeneous model with a reconstructed microstructure compared to the homogenous models with averaged values for the physical parameters is that a better understanding of the effects of microstructure on the cell performance can be achieved, allowing for a comprehensive assessment of the performance barriers, specifically the SE/AM interface challenge. For instance, the simulation showed that the lithium ions in the SE and AM have an inhomogeneous distribution specifically at lower pressing pressures which may cause cell degradation. Comparing homogenous 1D and heterogeneous 3D model results demonstrated that, although the predicted voltage profiles are almost identical, the 3D model predicts higher ohmic losses due to the consideration of the electrode microstructure. Notably, at high current rates, the heterogeneity has a higher impact on the electrochemical property distributions where lithium ion concentrations have a wider distribution range. The SE voltage drop distribution analysis depicted

that at low pressing pressure the SE voltage drop is about twice that at high pressing pressure. It was also shown that in addition to the AM particle shape, which has a significant effect on current density distribution at the interface with the SE, the void spaces also play a critical role, i.e. current density peaks happen at the neck of sandglass microstructures and least near void spaces. Overall, the presented 3D heterogeneous model sheds light on all aforementioned ASSBs' critical challenges and is a useful tool to address the effects of microstructural heterogeneity on cell behavior.

Acknowledgments

The authors thank Zachary P. Cano for the comprehensive review of the manuscript. This work was supported by the US National Science Foundation under Grant 1335850 and used resources of the Advanced Photon Source, a U.S. Department of Energy (DOE) Office of Science User Facility operated for the DOE Office of Science by Argonne National Laboratory under Contract DE-AC02-06CH11357. This research was also supported by the Natural Sciences and Engineering Research Council of Canada (NSERC) through grants to Z.C. and the University of Waterloo.

ORCID

Hamed Fathiannasab  <https://orcid.org/0000-0002-2416-139X>
 Zhongwei Chen  <https://orcid.org/0000-0003-3463-5509>

References

1. G. Zubi, R. Dufo-López, M. Carvalho, and G. Pasaoglu, "The lithium-ion battery: state of the art and future perspective." *Renew. Sustain. Energy Rev.*, **89**, 292 (2018).
2. E. Foreman, W. Zakri, M. Hossein Sanatimoghaddam, A. Modjtahedi, S. Pathak, A. G. Kashkooli, N. G. Garafolo, and S. Farhad, "A review of inactive materials and components of flexible lithium-ion batteries." *Adv. Sustain. Syst.*, **1**, 1700061 (2017).

3. F. Lv, Z. Wang, L. Shi, J. Zhu, K. Edström, J. Mindemark, and S. Yuan, "Challenges and development of composite solid-state electrolytes for high-performance lithium ion batteries." *J. Power Sources*, **441**, 227175 (2019).
4. P. H. Notten, F. Roozeboom, R. A. Niessen, and L. Baggetto, "3-D integrated all-solid-state rechargeable batteries." *Adv. Mater.*, **19**, 4564 (2007).
5. T. F. Miller III, Z.-G. Wang, G. W. Coates, and N. P. Balsara, "Designing polymer electrolytes for safe and high capacity rechargeable lithium batteries." *Acc. Chem. Res.*, **50**, 590 (2017).
6. Q. Li, T. Yi, X. Wang, H. Pan, B. Quan, T. Liang, X. Guo, X. Yu, H. Wang, and X. Huang, "In-situ visualization of lithium plating in all-solid-state lithium-metal battery." *Nano Energy*, **63**, 103895 (2019).
7. W. Ping, C. Yang, Y. Bao, C. Wang, H. Xie, E. Hitz, J. Cheng, T. Li, and L. Hu, "A silicon anode for garnet-based all-solid-state batteries: interfaces and nanomechanics." *Energy Storage Mater.*, **21**, 246 (2019).
8. K. Takada, "Progress and prospective of solid-state lithium batteries." *Acta Mater.*, **61**, 759 (2013).
9. J. G. Kim, B. Son, S. Mukherjee, N. Schuppert, A. Bates, O. Kwon, M. J. Choi, H. Y. Chung, and S. Park, "A review of lithium and non-lithium based solid state batteries." *J. Power Sources*, **282**, 299 (2015).
10. S. Choi, M. Jeon, J. Ahn, W. D. Jung, S. M. Choi, J.-S. Kim, J. Lim, Y.-J. Jang, H.-G. Jung, and J.-H. Lee, "Quantitative analysis of microstructures and reaction interfaces on composite cathodes in all-solid-state batteries using a three-dimensional reconstruction technique." *ACS Applied Materials & Interfaces*, **10**, 23740 (2018).
11. T. Li, H. Kang, X. Zhou, C. Lim, B. Yan, V. De Andrade, F. De Carlo, and L. Zhu, "Three-dimensional reconstruction and analysis of all-solid li-ion battery electrode using synchrotron transmission X-ray microscopy tomography." *ACS Applied Materials & Interfaces*, **10**, 16927 (2018).
12. N. Kazemi, D. L. Danilov, L. Haverkate, N. J. Dudney, S. Unnikrishnan, and P. H. Notten, "Modeling of all-solid-state thin-film Li-ion batteries: accuracy improvement." *Solid State Ionics*, **334**, 111 (2019).
13. D. Danilov, R. Niessen, and P. Notten, "Modeling all-solid-state Li-ion batteries." *J. Electrochem. Soc.*, **158**, A215 (2011).
14. S. D. Fabre, D. Guy-Bouyssou, P. Bouillon, F. Le Cras, and C. Delacourt, "Charge/discharge simulation of an all-solid-state thin-film battery using a one-dimensional model." *J. Electrochem. Soc.*, **159**, A104 (2011).
15. L. Raijmakers, D. Danilov, R.-A. Eichel, and P. Notten, "An advanced all-solid-state Li-ion battery model." *Electrochimica Acta*, **330**, 135147 (2019).
16. N. Wolff, F. Röder, and U. Krewer, "Model based assessment of performance of lithium-ion batteries using single ion conducting electrolytes." *Electrochim. Acta*, **284**, 639 (2018).
17. A. Bates, S. Mukherjee, N. Schuppert, B. Son, J. G. Kim, and S. Park, "Modeling and simulation of 2D lithium-ion solid state battery." *Int. J. Energy Res.*, **39**, 1505 (2015).
18. T. M. Clancy and J. F. Rohan, "Simulations of 3D nanoscale architectures and electrolyte characteristics for Li-ion microbatteries." *Journal of Energy Storage*, **23**, 1 (2019).
19. M. Biton, V. Yufit, F. Tariq, M. Kishimoto, and N. Brandon, "Enhanced imaging of lithium ion battery electrode materials." *J. Electrochem. Soc.*, **164**, A6032 (2017).
20. T. Hutzenlaub, S. Thiele, N. Paust, R. Spotnitz, R. Zengerle, and C. Walchshofer, "Threedimensional electrochemical Li-ion battery modelling featuring a focused ion-beam/scanning electron microscopy based three-phase reconstruction of a LiCoO₂ cathode." *Electrochim. Acta*, **115**, 131 (2014).
21. A. J. Ilott, M. Mohammadi, H. J. Chang, C. P. Grey, and A. Jerschow, "Real-time 3D imaging of microstructure growth in battery cells using indirect MRI." *Proc. Natl Acad. Sci.*, **113**, 10779 (2016).
22. A. G. Kashkooli, S. Farhad, D. U. Lee, K. Feng, S. Litster, S. K. Babu, L. Zhu, and Z. Chen, "Multiscale modeling of lithium-ion battery electrodes based on nanoscale X-ray computed tomography." *J. Power Sources*, **307**, 496 (2016).
23. A. G. Kashkooli, E. Foreman, S. Farhad, D. U. Lee, W. Ahn, K. Feng, V. De Andrade, and Z. Chen, "Synchrotron X-ray nano computed tomography based simulation of stress evolution in LiMn₂O₄ electrodes." *Electrochim. Acta*, **247**, 1103 (2017).
24. A. G. Kashkooli, E. Foreman, S. Farhad, D. U. Lee, K. Feng, G. Lui, V. De Andrade, and Z. Chen, "Morphological and electrochemical characterization of nanostructured Li₄Ti₅O₁₂ electrodes using multiple imaging mode synchrotron X-ray computed tomography." *J. Electrochem. Soc.*, **164**, A2861 (2017).
25. A. Ghorbani Kashkooli, *Nanoscale X-ray computed tomography based modeling of lithium-ion battery electrodes*, University of Waterloo (2018), UWSPACE, <http://hdl.handle.net/10012/12826>.
26. S. Lee, J. Tam, W. Li, B. Yu, H. J. Cho, J. Samei, D. S. Wilkinson, H. Choe, and U. Erb, "Multi-scale morphological characterization of Ni foams with directional pores." *Mater. Charact.*, 109939 (2019).
27. O. O. Taiwo, D. P. Finegan, D. S. Eastwood, J. L. Fife, L. D. Brown, J. A. Darr, P. D. Lee, D. J. Brett, and P. R. Shearing, "Comparison of three-dimensional analysis and stereological techniques for quantifying lithium-ion battery electrode microstructures." *J. Microsc.*, **263**, 280 (2016).
28. F. Tariq, V. Yufit, M. Kishimoto, P. Shearing, S. Menkin, D. Golodnitsky, J. Gelb, E. Peled, and N. Brandon, "Three-dimensional high resolution X-ray imaging and quantification of lithium ion battery mesocarbon microbead anodes." *J. Power Sources*, **248**, 1014 (2014).
29. R. Banerjee, N. Bevilacqua, A. Mohseninia, B. Wiedemann, F. Wilhelm, J. Scholta, and R. Zeis, "Carbon felt electrodes for redox flow battery: Impact of compression on transport properties." *Journal of Energy Storage*, **26**, 100997 (2019).
30. J. Tippens, J. Miers, A. Afshar, J. Lewis, F. J. Q. Cortes, H. Qiao, T. S. Marchese, C. V. Di Leo, C. Saldana, and M. T. McDowell, "Visualizing chemo-mechanical degradation of a solid-state battery electrolyte." *ACS Energy Lett.*, **4**, 1475 (2019).
31. S. Choi, B.-N. Yun, W. D. Jung, T. H. Kim, K.-Y. Chung, J.-W. Son, B.-I. Sang, H.-G. Jung, and H. Kim, "Tomographical analysis of electrochemical lithiation and delithiation of LiNi_{0.6}Co_{0.2}Mn_{0.2}O₂ cathodes in all-solid-state batteries." *Scr. Mater.*, **165**, 10 (2019).
32. N. M. Asl, J. Keith, C. Lim, L. Zhu, and Y. Kim, "Inorganic solid/organic liquid hybrid electrolyte for use in Li-ion battery." *Electrochim. Acta*, **79**, 8 (2012).
33. B. Tjaden, S. J. Cooper, D. J. Brett, D. Kramer, and P. R. Shearing, "On the origin and application of the Bruggeman correlation for analysing transport phenomena in electrochemical systems." *Current Opinion in Chemical Engineering*, **12**, 44 (2016).
34. V. D. Bruggeman, "Berechnung verschiedener physikalischer Konstanten von heterogenen Substanzen. I. Dielektrizitätskonstanten und Leitfähigkeiten der Mischkörper aus isotropen Substanzen." *Ann. Phys.*, **416**, 636 (1935).
35. S. Cooper, D. Eastwood, J. Gelb, G. Dambanc, D. Brett, R. Bradley, P. Withers, P. Lee, A. Marquis, and N. Brandon, "Image based modelling of microstructural heterogeneity in LiFePO₄ electrodes for Li-ion batteries." *J. Power Sources*, **247**, 1033 (2014).
36. M.-C. Pang, Y. Hao, M. Marinescu, H. Wang, M. Chen, and G. J. Offer, "Experimental and numerical analysis to identify the performance limiting mechanisms in solid-state lithium cells under pulse operating conditions." *Phys. Chem. Chem. Phys.*, **21**, 22740 (2019).
37. A. Ghorbani Kashkooli, E. Foreman, S. Farhad, D. U. Lee, W. Ahn, K. Feng, V. De Andrade, and Z. Chen, "Synchrotron X-ray nano computed tomography based simulation of stress evolution in LiMn₂O₄ electrodes." *Electrochim. Acta*, **247** (Supplement C), 1103 (2017).
38. A. N. Mistry, K. Smith, and P. P. Mukherjee, "Secondary-phase stochastics in lithium-ion battery electrodes." *ACS Applied Materials & Interfaces*, **10**, 6317 (2018).
39. A. G. Kashkooli, A. Amirfazli, S. Farhad, D. U. Lee, S. Felicelli, H. W. Park, K. Feng, V. De Andrade, and Z. Chen, "Representative volume element model of lithium-ion battery electrodes based on X-ray nano-tomography." *J. Appl. Electrochem.*, **47**, 281 (2017).
40. S.-L. Wu, W. Zhang, X. Song, A. K. Shukla, G. Liu, V. Battaglia, and V. Srinivasan, "High rate capability of Li (Ni_{1/3}Mn_{1/3}Co_{1/3}) O₂ electrode for Li-ion batteries." *J. Electrochem. Soc.*, **159**, A438 (2012).
41. P. Knauth, "Inorganic solid Li ion conductors: an overview." *Solid State Ionics*, **180**, 911 (2009).
42. Y. Zhao, P. Stein, Y. Bai, M. Al-Siraj, Y. Yang, and B.-X. Xu, "A review on modeling of electro-chemo-mechanics in lithium-ion batteries." *J. Power Sources*, **413**, 259 (2019).
43. B. L. Trembacki, A. N. Mistry, D. R. Noble, M. E. Ferraro, P. P. Mukherjee, and S. A. Roberts, "Mesoscale analysis of conductive binder domain morphology in lithium-ion battery electrodes." *J. Electrochem. Soc.*, **165**, E725 (2018).
44. L. Wu, X. Xiao, Y. Wen, and J. Zhang, "Three-dimensional finite element study on stress generation in synchrotron X-ray tomography reconstructed nickel-manganese-cobalt based half cell." *J. Power Sources*, **336**, 8 (2016).
45. D. Hlushkou, A. E. Reising, N. Kaiser, S. Spannenberger, S. Schlabach, Y. Kato, B. Roling, and U. Tallarek, "The influence of void space on ion transport in a composite cathode for all-solidstate batteries." *J. Power Sources*, **396**, 363 (2018).
46. R. Koerver, I. Aygün, T. Leichtweiß, C. Dietrich, W. Zhang, J. O. Binder, P. Hartmann, W. G. Zeier, and J. R. Janek, "Capacity fade in solid-state batteries: interphase formation and chemomechanical processes in nickel-rich layered oxide cathodes and lithium thiophosphate solid electrolytes." *Chem. Mater.*, **29**, 5574 (2017).
47. G. Bucci, T. Swamy, Y.-M. Chiang, and W. C. Carter, "Modeling of internal mechanical failure of all-solid-state batteries during electrochemical cycling, and implications for battery design." *Journal of Materials Chemistry A*, **5**, 19422 (2017).